DISTRIBUTED DISLOCATION METHOD FOR DETERMINING ELASTIC FIELDS OF 2D AND 3D VOLUME MISFIT PARTICLES IN INFINITE SPACE AND EXTENSION OF THE METHOD FOR PARTICLES IN HALF SPACE

J. D. Lerma T. Khraishi [*] S. Kataria Y.-L. Shen

Department of Mechanical Engineering
University of New Mexico
New Mexico, USA

ABSTRACT

A multitude of researchers have utilized a variety of techniques to formulate the stresses and deformations caused by volume misfit inclusions in infinite host media. Few of such techniques can also be extended to derive solutions for inclusions in a half space. In this manuscript we present a novel computational method for determining the elastic fields of two and three-dimensional inclusions of arbitrary shape in an infinite host matrix. The misfit strain is treated by a distribution of prismatic dislocation loops. A systematic numerical assessment illustrates that the discretization can yield excellent agreement with existing analytical solutions for certain particle geometries. This method is then further developed to solve for two-dimensional problems in a half space.

Keywords: Eigenstrain, Distributed dislocations, Half space, Elastic field.

1. INTRODUCTION

Precipitates in alloys may acquire a variety of geometrical shapes such as spheres, cuboids, and ellipses among others. The volume misfit between the precipitates and the host matrix result in internal stresses, which consequently dramatically influence the alloy's mechanical properties. Such lattice mismatches may be a result of thermal expansion or contraction, phase transformations, plastic deformation, *etc*. Many different approaches for computing the elastic fields generated by such particles in an infinite host matrix have been developed. One method is the boundary-value problem (BVP), which was demonstrated by Teodosiu [1] when solving for the cases of spherical and cylindrical misfit particles of uniform radial misfit. Bert *et al*. [2] obtained the elastic stresses, strains, and displacements for a sphere inclusion with a one axis dilatation utilizing the eigenstrain method, also referred to as the Eshelby procedure [3,4]. The Green function method is another manner by which to solve for these kinds of problems. This method was demonstrated by Pearson and Faux [5] when solving for strain fields of pyramidal quantum dots. Also, Andreev *et al*. [6] determined the strain fields of quantum dots of arbitrary shape using the Green function method. Lastly, the method of infinitesimal inclusions, briefly described by Sheinerman and Ovid'co [7], can be used.

The problem of determining the elastic field caused by inclusions in half space is also of great interest in engineering and has been subject of numerous investigations. Amongst the first to study the elastic fields in a semi-infinite space was Melan [8], who constituted analytical solutions for the two dimensional case of a concentrated point force in a homogeneous and isotropic half space. A few years later Mindlin [9] generalized the solution of that problem for the three dimensional case. With the aid of Mindlin's aforementioned solutions and the process of superposition, Mindlin and Cheng [10] were then able to derive the stress functions for nuclei of strain which they then utilized to solve for the case of a thermally expanding spherical inclusion adjacent to a free surface (Mindlin and Cheng, [11]). Moreover, Aderogba [12] was able to generalize Mindlin and Cheng's findings for inclusions with arbitrary eigenstrains. Inclusion particles of various other configurations have also been subject of study. For example, Chiu [13] presented the closed form solutions for the stresses and surface deformations generated by a cuboidal inclusion with uniform eigenstrains while Hu [14] used the concept of nucleus of thermal strain to obtain analytical solutions for a parallelepipedic thermal inclusion in a three dimensional semi-space. Work with reference to ellipsoidal inclusions in half space has been executed by Seo and Mura [15] as well as by Masumura and Chou [16] among others. Hasegawa *et al*. [17] found the exact closed-form solutions for the axisymmetric elastic fields caused by a solid or hollow cylindrical inclusion in a half-space. Wu and Du [18] also solved the cylindrical inclusion problem in an elastic half space using the Green's function technique. Using conformal map-

[*] Corresponding author (khraishi@unm.edu)

DOI : 10.1017/jmech.2014.85
Copyright © 2014 The Society of Theoretical and Applied Mechanics, R.O.C.
https://doi.org/10.1017/jmech.2014.85 Published online by Cambridge University Press

ping and analytical continuation Ru [19] became one of the first to present analytical solutions for inclusions of arbitrary shape. Invaluable contributions regarding quantum dots and quantum wires, of various geometries, in a half space have also been made by investigators such as Glas [20-24], Romanov *et al*. [25], and Pan and Yang [26].

The problem with the previously mentioned techniques is that typically the solution has to be reformulated every time the geometry of the problem is changed, which gives rise to "The Distributed Dislocation Method" introduced here. This new method is unique in that it can effectively be applied to solve for the elastic field of inclusions of any given shape without having to reformulate if the geometry is altered. This is very convenient when studying problems which encompass complex and irregular inclusions. It is also applicable to particles with non-uniform eigenstrains.

2. PROCEDURE

The eigenstrain problem posed by the misfit strain, *i.e.* volumetric misfit strain, is treated via a distribution of prismatic dislocation loops. Each of these prismatic dislocation loops acts as an extra plane of atoms inserted inside the host matrix, as demonstrated by Hirth and Lothe [27] and Hull and Bacon [28], hence causing local misfit. The magnitude of the Burgers vector, $\boldsymbol{b}$, of each loop along a particular direction contributes towards the total amount of misfit.

2.1 Two-Dimensional Particles in Infinite Space

We begin by finding the elastic field of an infinitely long cylindrical misfit particle/inclusion embedded in an infinite matrix. Figure 1 shows a cross section of the problem. An orthogonal coordinate system is utilized, where the z-axis extends along the length of the particle/inclusion. Here the particle has a radius r_0, and a continuous radial misfit δ. For simplicity the shear modulus, μ, and Poisson ratio, ν, were considered to be equal for the particle/inclusion and the surrounding matrix. The elastic field is to be found at any given point $P(x, y)$.

As previously mentioned, the eigenstrain problem posed by the misfit strain is treated via a distribution of prismatic dislocation loops. For instance, assume a particle has an associated eigenstrain in the x-direction (*i.e.*, e^*_{xx}), then to emulate such strain a uniform distribution of polygonal prismatic dislocation loops is put in place along the x-axis (in y-z planes) of the particle. The perimeter of these loops coincide with the particle surface. If the eigenstrain is e^*_{yy} instead, then the loop distribution will be along the y-axis (in x-z planes). The same approach applies to the z-direction. If a combination of eigenstrains exists, then the total effect is simply obtained by superposition. Since an infinitely long particle with a radial misfit is considered first, only eigenstrains in the x- and y-directions are considered.

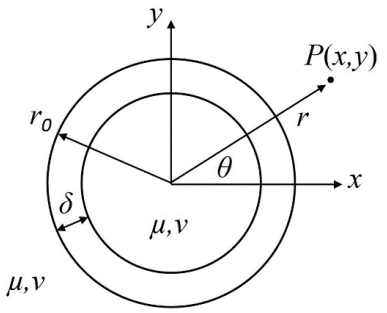


Fig. 1 Cross-section of infinitely long volume misfit cylindrical particle/inclusion. The particle has a radius r_0 and there is a continuous radial misfit of δ around the particle/inclusion. This figure could also represent the cross section of a volume misfit spherical particle/inclusion.

The problem is thus solved by discretizing the particle, shown in Fig. 2(a), into M by N prismatic interstitial dislocation loops which are regularly distributed along y-z and x-z planes, respectively, as shown in Fig. 2(b). This type of discretization may be referred to as an $M \times N$ mesh. In the figure, the particle is represented with three dislocation loops along three y-z planes ($M = 3$) and three loops on three x-z planes ($N = 3$), or in other words, a 3×3 mesh where $M = N$. For this particular problem each loop consists of four edge dislocation segments and is rectangular in shape.

For each loop, the dislocation segments on the x-y planes, the shorter dislocation segments in Fig. 2(b), are ignored since they are assumed to be located at $+\infty$ and $-\infty$ and do not contribute to the state of elastic deformation in the material. Figure 2(c) is a cross section of the discretized particle of Fig. 2(b). In this figure the vertical and horizontal lines within the representative particle outline correspond to the cross sections of the dislocation loops (*i.e.*, the cross sections of the horizontal and vertical interstitial planes of atoms). Here each dislocation loop is now represented by two oppositely-signed and infinite edge dislocations, where the smaller circles with the crosses and the dots in the center indicate the inward (into the page) and outward dislocation line directions, respectively.

From the principle of superposition, the total elastic fields at any given point $P(x, y)$ is determined by summing the contributions of each individual dislocation at that point, as demonstrated in Eq. (1) for the displacement field. In the past a similar numerical approach for determining the elastic field of such a particle was presented by Lerma *et al*. [29].

$$\boldsymbol{u}^P = \sum_{i=1}^{2(M+N)} \boldsymbol{u}^i = \sum_{i=1}^{2(M+N)} (\boldsymbol{u}^i_x + \boldsymbol{u}^i_y) \tag{1}$$

where i is a loop counter and the superscript P refers to the field point of interest.

In the specific case of the cylindrical inclusion from Fig. 1 it is observed that the total linear misfits along both the x and y directions, which shall be respectively known as δx and δy, are both equivalent to 2δ. In the

https://doi.org/10.1017/jmech.2014.85 Published online by Cambridge University Press

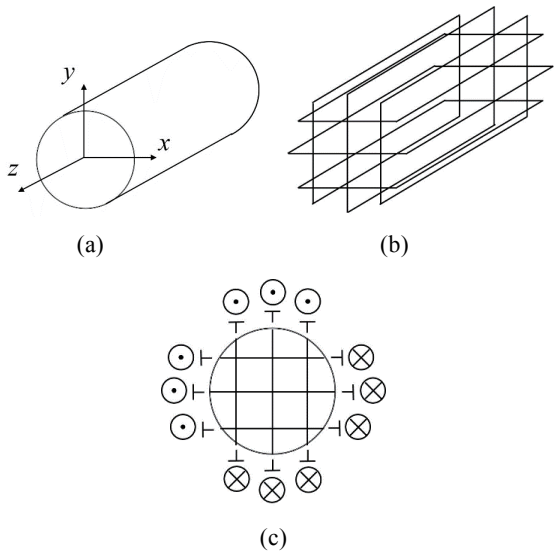


Fig. 2 (a) Section of the continuous misfit particle, surrounded by a matrix of equal elastic constants. (b) Discretization of the particle volume into localized misfit regions (3 × 3 mesh) each representing a dislocation loop. (c) Cross section of the discretized particle in (b).

numerical method presented here, such directional misfits are directly related to the prescribed "thicknesses" of the individual interstitial dislocation loops, or more precisely, to their Burgers vector magnitude. Essentially, the total misfit in either direction (x, y, or z) is equal to the sum of the Burgers vectors of the prismatic dislocation loops whose normal vector points in that direction. In the case depicted in Fig. 2(b), for instance, δx is equal to the sum of the Burgers vectors magnitudes of the dislocation loops on the three y-z planes.

2.2 Three-Dimensional Particles in Infinite Space

The method for determining the elastic fields of three-dimensional particle inclusions in infinite space is fundamentally the same as that of the two-dimensional ones. The chief difference is that there is now an aggregation of normal eigenstrains in all three directions. Figure 3 illustrates the volumetric eigenstrain represented by the distribution of dislocation loops along x, y and z directions for a spherical inclusion. Each loop is now a circular polygon consisting of 32 continuous linear dislocation segments. Again, to find the total elastic field one simply has to sum the elastic fields of all the loops. Also, in Fig. 3 the spherical particle has a diameter L = 10000 units, where units can be chosen arbitrarily. This is because we present our results in normalized form, *i.e.*, the results we present here are valid irrespective of dimensions of these particle.

With regard to the Burgers vector magnitude of each loop, b, it is simply obtained using the following equation:

$$bN = L\,e^{*}$$

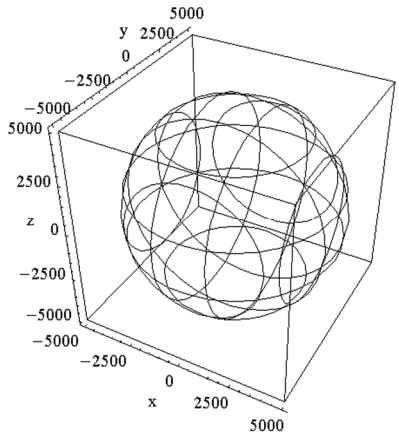


Fig. 3 Representation of a spherical particle inclusion using a 4 × 4 × 4 mesh.

where N is the total number of loops, L is the physical length, and e^{*} is the corresponding normal strain along the direction of interest (*i.e.* x, y or z). A more accurate representation of the inclusion is obtained when N is large, and correspondingly b is small.

As mentioned above, each circular dislocation loop is comprised of a series of linear dislocation segments. Hence the method utilizes the results of a previous work by Devincre [30] which gives the expression for the stress field of a half dislocation line, shown in Fig. 4. The stress field is given by:

$$\sigma_{ij}(r) = \frac{\mu}{\pi Y^2}\left[[\boldsymbol{bYt}]^{s}_{ij} - \frac{1}{(1-\nu)}[\boldsymbol{b\,t\,Y}]^{s}_{ij} - \frac{(\boldsymbol{b},\boldsymbol{Y},\boldsymbol{t})}{2(1-\nu)}\left[\delta_{ij} + t_i\,t_j + \frac{2}{Y^2}\left[\rho_i Y_j + \rho_j Y_i + \frac{L'}{R} Y_i\,Y_j \right] \right] \right]$$

where

$$\boldsymbol{R} = \boldsymbol{r} - \boldsymbol{r}',$$
$$L' = \boldsymbol{R}\cdot\boldsymbol{t},$$
$$\boldsymbol{\rho} = \boldsymbol{R} - L'\boldsymbol{t},$$
$$\boldsymbol{Y} = \boldsymbol{R} + R\boldsymbol{t}$$
$$[\boldsymbol{lmn}]^{s}_{ij} = \frac{1}{2}\left((\boldsymbol{l}\times\boldsymbol{m})_i\,n_j + (\boldsymbol{l}\times\boldsymbol{m})_j\,n_i \right),$$
$$(\boldsymbol{l},\boldsymbol{m},\boldsymbol{n}) = \boldsymbol{n}\cdot(\boldsymbol{l}\times\boldsymbol{m}),$$

$\boldsymbol{b}$ is the dislocation's Burgers Vector and $\boldsymbol{t}$ is the line sense. The superscript s indicates that the square bracketed terms are operated upon to produce a second rank symmetric tensor (see defining equation).

The stress field of a finite straight dislocation segment lying between points A and B, shown in Fig. 4, is then obtained by subtracting the results of the above equation at the two points, *i.e.*

$$\sigma^{AB}_{ij}(\boldsymbol{r}) = \sigma_{ij}(\boldsymbol{r})_{r'=B} - \sigma_{ij}(\boldsymbol{r})_{r'=A}$$

Applying the summation over a closed polygonal loop consisting of finite dislocation segments, which represents a misfit atomic plane, the stress field due to a dislocation loop can be found. For example Fig. 5 shows one rectangular loop with Burgers vector pointing perpendicular to its habit plane.

https://doi.org/10.1017/jmech.2014.85 Published online by Cambridge University Press

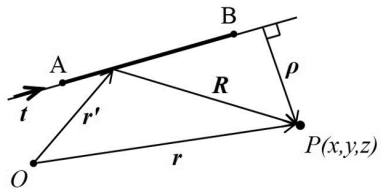


Fig. 4 *AB* represents a finite linear dislocation segment, ***t*** is the line sense vector along *AB*, ***r***′ and ***r*** are the position vectors of any point on the segment *AB* and a material/field point *P*, respectively, w.r.t. origin *O*, ρ is a vector perpendicular to the segment *AB* when extended along ***t***.

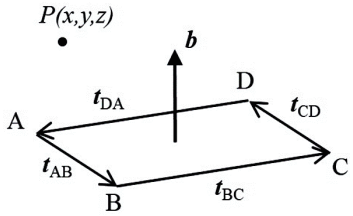


Fig. 5 A rectangular prismatic loop consisting of four dislocation line segments *AB*, *BC*, *CD*, and *DA*.

The loop consists of four dislocation segments *AB*, *BC*, *CD* and *DA*, which are all edge in character. The point *P* in the figure represents any arbitrary point at which we wish to calculate the elastic fields due to the loop volume misfit. The point can lie inside or outside the particle. The strength of stress field at this material point is proportional to its distance from the loop. Now the stress field expression at this point *P* is found by the summation of individual expressions due to each dislocation segment in Fig. 5, *i.e.*

$$\sigma_{ij}^{ABCD} = \sigma_{ij}^{AB} + \sigma_{ij}^{BC} + \sigma_{ij}^{CD} + \sigma_{ij}^{DA}$$

2.3 Two-Dimensional Particles in Half Space

The problem to be solved is depicted on Fig. 6(a), which shows the cross section of an infinitely long misfit cylindrical particle of radius r_0 with a continuous radial misfit δ. The center of the particle is at a distance *d* from the free surface. An orthogonal coordinate system is utilized, where the isotropic elastic medium is defined by the semi-infinite domain $y \le 0$ and the *z*-axis runs parallel to the length of the inclusion. We are interested in determining the elastic fields at any arbitrary point $P(x, y)$.

In order to proceed it is first necessary to derive solutions for a single infinitely long dislocation in a half space. According to Bacon and Groves [31] the displacement field at a point *P* generated by an infinitesimal dislocation loop at a distance c below a free surface in an isotropic elastic half medium, as shown in Fig. 7, is described by Eq. (2).

$$d\mathbf{u} = d\mathbf{u}^{inf} + d\mathbf{u}^{image} + d\mathbf{u}^{s} \tag{2}$$

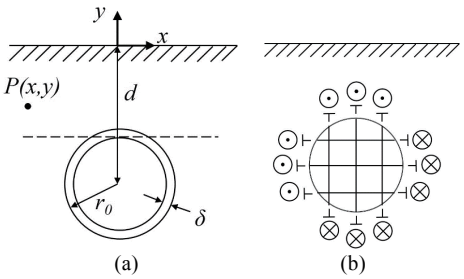


Fig. 6 (a) Cross section of a cylindrical misfit particle of radius r_0 with its center at a distance *d* from a free surface. The dashed line parallel to the free surface and tangent to the particle represents an internal surface along which results are plotted later in the paper. (b) Same particle now discretized into six prismatic dislocation loops.

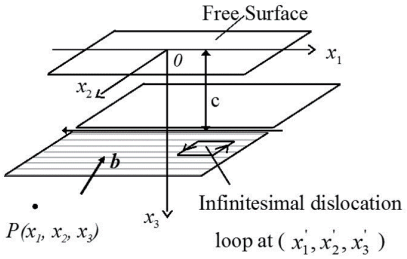


Fig. 7 This figure shows an infinitely long dislocation line with arbitrary Burgers vector *b*. The line is a distance *c* below the surface and is parallel to it. The correction terms are obtained by integration over the shaded area.

Here the term with the "*inf*" superscript correspond to a sub-surface loop with Burgers vector ***b*** as if it were in an infinite media, the terms with the "*image*" superscript correspond to a mirror image dislocation loop at a distance c above the free surface with negative Burgers vector, and the terms with an "*s*" superscript correspond to the surface correction terms which ensure zero traction at the surface.

As demonstrated by Jing [32], the displacement correction term $\boldsymbol{u}^s$ for a finite-sized dislocation loop may be found by Eq. (3), where *A* is the area of the loop and $d\boldsymbol{u}^s$ is shown in Eq. (4), as provided by Bacon and Groves [31].

$$\boldsymbol{u}^s = \iint_A d\boldsymbol{u}^s \tag{3}$$

$$du_i^s = kx_3'(1-2\delta_{j3})\left[A_{i3}\left(\frac{1}{R}\right)_{,ij} - \left(\frac{x_3}{R}\right)_{,ij3}\right] \tag{4}$$

Here

$$k = b_j\, dS / 4\pi(1-\nu)\,,\quad dS = dx_1'\, dx_2'\,,$$
$$A_{ij} = 2\nu + 4(1-\nu)\,\delta_{ij}$$
$$R^2 = (x_1 - x_1')^2 + (x_2 - x_2')^2 + (x_3 - x_3')^2$$

Jing [32] also showed that if instead of integrating

https://doi.org/10.1017/jmech.2014.85 Published online by Cambridge University Press

Eq. (3) over area A, it is integrated over $dx_1' \to (-\infty, +\infty)$ and $dx_2' \to (0, +\infty)$, the shaded area in Fig. 7, the surface correction term for an infinitely long dislocation line beneath and parallel to a free surface can be obtained. The displacement field for such a dislocation line is then described by $\boldsymbol{u} = \boldsymbol{u}^{inf} + \boldsymbol{u}^{image} + \boldsymbol{u}^{s}$. Here $\boldsymbol{u}^{inf}$ is the displacement field of an infinitely long edge dislocation in an infinite medium as given by Weertman [33]. Performing the aforementioned integration and summation for the said infinitely long subsurface dislocation line, shown in Fig. 7, as well as transforming from the (x_1, x_2, x_3) coordinate system to our (x, y, z) system yields Eqs. 5 and 6 below. In these equations the position of dislocation i is given by the coordinates (x_i, y_i), where $y_i = c_i$ and ν is Poison's ratio. The problem described in Fig. 6 is then solved by superposition of the elastic fields of the infinite dislocations comprising the discretized particle.

$$u_y^i = b_x^i \frac{\left\{ \begin{array}{l} 4y_i \left\{ \begin{array}{l} (y-y_i)^2 (y+y_i)^2 \left[-3y - 2y_i + 2(y+y_i)\,\nu \right] \\ +2(x-x_i)^2 (y^2+y_i^2) \left[-y - 2y_i + 2(y+y_i)\,\nu \right] + (x-x_i)^4 \left[y - 2y_i + 2(y+y_i)\,\nu \right] \end{array} \right\} \\ +\left[(x-x_i)^2 + (y-y_i)^2 \right] \left[(x-x_i)^2 + (y+y_i)^2 \right]^2 (2\nu - 1) \left\{ \begin{array}{l} \log\left[(x-x_i)^2 + (y-y_i)^2 \right] \\ -\log\left[(x-x_i)^2 + (y+y_i)^2 \right] \end{array} \right\} \end{array} \right\}}{8\pi \left[(x-x_i)^2 + (y-y_i)^2 \right] \left[(x-x_i)^2 + (y+y_i)^2 \right]^2 (\nu - 1)}$$
$$+ b_y^i \frac{\left\{ \begin{array}{l} 2(x-x_i) y_i \left\{ \begin{array}{l} -2(x-x_i)^2 (y^2 + y y_i + y_i^2) + (y-y_i)(y+y_i) \left[2y y_i + y^2(\nu - 1) - y_i^2 (\nu - 1) \right] \\ +(x-x_i)^4 (\nu - 1) + 2(x-x_i)^2 (y^2 + y_i^2)\,\nu \end{array} \right\} \\ -\left[(x-x_i)^2 + (y-y_i)^2 \right] \left[(x-x_i)^2 + (y+y_i)^2 \right]^2 (\nu - 1) \left[\tan^{-1}\left(\frac{x-x_i}{y-y_i} \right) - \tan^{-1}\left(\frac{x-x_i}{y+y_i} \right) \right] \end{array} \right\}}{2\pi \left[(x-x_i)^2 + (y-y_i)^2 \right] \left[(x-x_i)^2 + (y+y_i)^2 \right]^2 (\nu - 1)} \tag{5}$$

$$u_x^i = b_x^i \frac{\left\{ \begin{array}{l} 2(x-x_i) y_i \left\{ \begin{array}{l} -y^4 + \left[(x-x_i)^2 + y_i^2 \right]^2 \\ -\left\{ \left[(x-x_i)^2 + y^2 \right]^2 + 2\left[(x-x_i) - y \right] \left[(x-x_i) + y \right] y_i^2 + y_i^4 \right\} \nu \end{array} \right\} \\ +\left[(x-x_i)^2 + (y-y_i)^2 \right] \left[(x-x_i)^2 + (y+y_i)^2 \right]^2 (\nu - 1) \left[\tan^{-1}\left(\frac{y-y_i}{x-x_i} \right) - \tan^{-1}\left(\frac{y+y_i}{x-x_i} \right) \right] \end{array} \right\}}{2\pi \left[(x-x_i)^2 + (y-y_i)^2 \right] \left[(x-x_i)^2 + (y+y_i)^2 \right]^2 (\nu - 1)}$$
$$+ b_y^i \frac{\left\{ \begin{array}{l} 4y_i \left\{ \begin{array}{l} -2(x-x_i)^2 (y^3 - 2y^2 y_i + y y_i^2 + 2y_i^3) + 4(x-x_i)^2 (y+y_i)(y^2 + y_i^2)\,\nu \\ +(x-x_i)^4 \left[-y - 2y_i + 2(y+y_i)\,\nu \right] + (y-y_i)^2 (y+y_i)^2 \left[-y - 2y_i + 2(y+y_i)\,\nu \right] \end{array} \right\} \\ +\left[(x-x_i)^2 + (y-y_i)^2 \right] \left[(x-x_i)^2 + (y+y_i)^2 \right]^2 (2\nu - 1) \left\{ \begin{array}{l} \log\left[(x-x_i)^2 + (y-y_i)^2 \right] \\ -\log\left[(x-x_i)^2 + (y+y_i)^2 \right] \end{array} \right\} \end{array} \right\}}{8\pi \left[(x-x_i)^2 + (y-y_i)^2 \right] \left[(x-x_i)^2 + (y+y_i)^2 \right]^2 (\nu - 1)} \tag{6}$$

After finding the displacement field the stress and strain tensors are respectively via:

$$\sigma_{ij} = 2\mu \left(\varepsilon_{ij} + \frac{\nu}{1-2\nu} \varepsilon_{kk}\, \delta_{ij} \right) \text{ and } \varepsilon_{ij} = \frac{1}{2} \left(\frac{\partial u_i}{\partial x_j} + \frac{\partial u_j}{\partial x_i} \right)$$

Here δ_{ij} is the Kronecker delta.

3. RESULTS

3.1 Two-Dimensional Particles in Infinite Space: Cylinder and Ellipse

Results using the presented distributed dislocation method were obtained for a cylindrical particle as well as for an elliptical particle. The cylindrical particle used in the calculations had a radius $r_0 = 100b$. For the elliptical particle, the semimajor axis measured $200b$ while the semiminor axis was $100b$. Here b is the Burgers vector magnitude, which is equal to one for simplicity. For both the cylindrical and the elliptical problems the Poisson ratio was $\nu = 0.3$ for the particles and the surrounding matrix. The cylindrical particle was discretized into 30 loops along the x and y directions (30 × 30) while the elliptical into 30 loops along the y direction and 60 loops along the x direction (60 × 30). For both particles the eigenstrains were arbitrarily selected to be $e_{xx}^* = e_{yy}^* = 0.01$ and the re-

https://doi.org/10.1017/jmech.2014.85 Published online by Cambridge University Press

sults were normalized by the shear modulus μ.

For any results obtained to be valid, satisfaction of the equilibrium equations has to occur. Figure 8(a) shows satisfaction of one equilibrium equation, $\partial\sigma_{xx} / \sigma_x + \partial\sigma_{xy} / \sigma_y = 0$, over $x \rightarrow (-200, 200)$ and $y \rightarrow (-200, 200)$ for the cylindrical particle. Figure 8(b) also shows satisfaction of the same equilibrium equation now for the elliptical particle over $x \rightarrow (-400, 400)$ and $y \rightarrow (-400, 400)$.

Stress plots were subsequently obtained. To investigate how the loop density of the particles affected the numerical results, plots of the stress were obtained for particles discretized with increasing numbers of dislocation loops. This was done for both the cylindrical and the elliptical particles. Results were obtained along $(x, 0)$, where $x \rightarrow (r_0, 2r_0)$, for the cylindrical particle. Along this range it was observed that different results were obtained if the particle was discretized with even or odd numbers of dislocation loops. Figures 9(a) and 9(b) shows the resulting plots of σ_{xx} for the cylindrical particle discretized with increasing even and odd numbers of dislocation loops, respectively. Smaller dashes indicate higher loop densities. Here it is evident that numerical results better approximate the analytical solution (solid line) as the number of dislocation loops increases. When odd numbers of loops are utilized, it is observed that results continuously approach infinity when obtained closer to the particle-matrix interface. This occurs despite the use of high loop densities. The reason why this occurs has much to do with the chosen plot range. For the results shown here, it was decided to plot along the x axis. Every time the particle is discretized into odd numbers of loops, two dislocations are placed along the x axis. One example of this can be seen in Fig. 2(c), where the central horizontal plane of atoms runs along the x axis and is represented by the dislocations at each of its ends. Plotting near one of these dislocations will naturally cause results to verge toward infinity. When the particle is discretized with even numbers of loops there are no dislocations along the x axis and thus averting plotting near a dislocation.

Plots were then obtained for the elliptical particle along $(x, 0)$, where $x \rightarrow (0, 200)$. Figures 10(a) and 10(b) show the numerical results as the particle is discretized with increasing even and odd numbers of dislocation loops, respectively. As before, in these figures it can be observed that results better approximate the analytical solution (solid line) as the mesh density increases. Again, the plots in Fig. 10(b) approach infinity near the particle-matrix interface due to the chosen plot range, as explained previously.

Plots of the displacements were also obtained for the cylindrical and elliptical particles but are not shown here for brevity. The displacement plots also showed good agreement with analytical solutions.

3.2 Three-Dimensional Particles in Infinite Space: Sphere, Cube, and Cuboid

3.2.1 Sphere

Now the numerical results for a spherical particle, such as the one in Fig. 3, are presented and compared

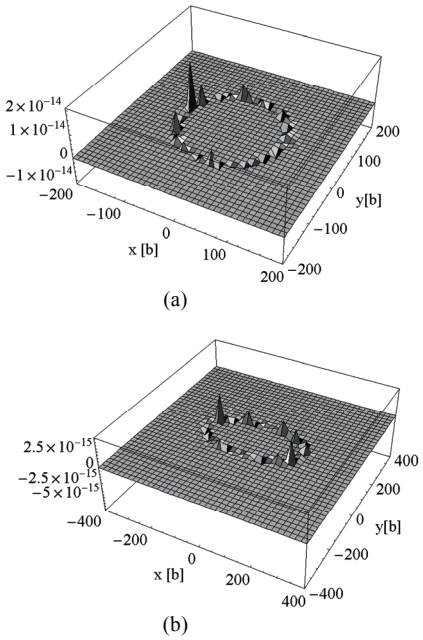


Fig. 8 (a) Satisfaction of one equilibrium equation over $x \rightarrow (-200, 200)$ and $y \rightarrow (-200, 200)$ for the cylindrical particle. (b) Satisfaction of an equilibrium equation for the elliptical particle over $x \rightarrow (-400, 400)$ and $y \rightarrow (-400, 400)$.

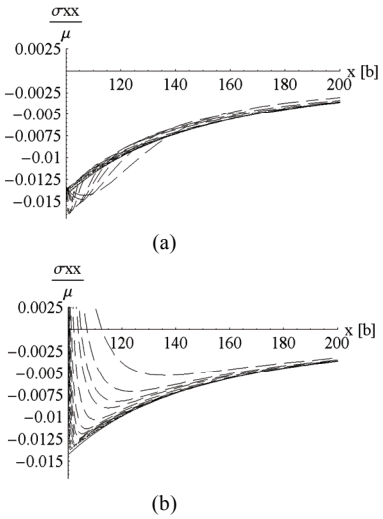


Fig. 9 Plots of σ_{xx} for the cylindrical particle discretized with increasing even (a) and odd (b) numbers of dislocation loops. Plots were obtained along $(x, 0)$, where $x \rightarrow (r_0, 2r_0)$.

with the available analytical solution by Teodosiu [1]. The results are presented in normalized form given that the analytical solution is also presented in normalized form. The normalization factor is Ee^* where,

$$E = \text{Young's Modulus} = 2\mu(1+\nu) \text{ and}$$
$$e^* = \text{eigenstrain} = (Nb) / L$$

Such normalized results can be used to determine the actual results by substituting the real values of the normalizing parameters. Varying mesh densities have

https://doi.org/10.1017/jmech.2014.85 Published online by Cambridge University Press

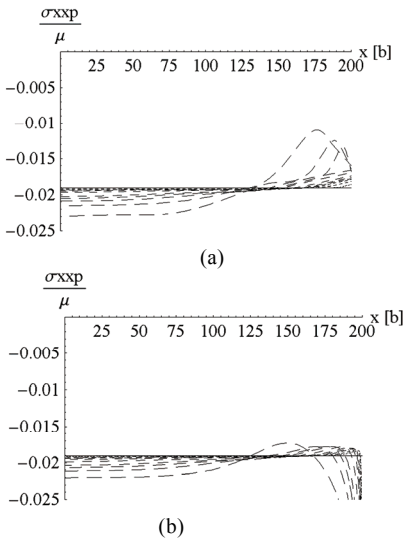


Fig. 10 Plots of σ_{xx} for the elliptical particle discretized with increasing even (a) and odd (b) numbers of dislocation loops. Plots were obtained along $(x, 0)$, where $x \rightarrow (0, 200)$.

been used, where the results presented here were obtained using $2 \times 2 \times 2$, $4 \times 4 \times 4$, $8 \times 8 \times 8$, $20 \times 20 \times 20$, $40 \times 40 \times 40$ and $80 \times 80 \times 80$ meshes. Figure 11 represents the normalized σ_{xx}, plotted along the x-axis. Here, the solid black line represents the analytical solution. From the figure it is clear that the numerical solution converges to the analytical solution with increasing loop densities, *i.e.*, the analytical solution and the results from the $80 \times 80 \times 80$ mesh nearly superimpose each other both inside and outside the particle. Interestingly, a "*kink*" is observed in the plots when approaching the precipitate-matrix interface. It is presumed that this occurs because results are being calculated very close to dislocation segments.

The effect that the number of segments per loops have on the results were investigated next. An $80 \times 80 \times 80$ mesh was established and the number of segments per loop examined were 10, 20, 30, 40, and 60. Figure 12 shows the results. Decreasing dash size for the plots denotes the increasing number of segments per loop. Again, the analytical solution is represented by the continuous curve.

It is clear from the figure that the numerical solution converges to the analytical solution with increasing number of segments per loop. Also, the kink near the boundary becomes more uniform about the *x*-direction, *i.e.*, the height of crest and trough becomes uniform with increasing number of segments per loop. Hence if we were to find the average about the center point of the kink, we would get the solution that matches the analytical solution at that point.

3.2.2 Cube and Cuboid

Now, the results of the Distributed Dislocation Method for perfect cubical (Fig. 13(a)) and cuboidal (*i.e.* cube with chamfered corners, Fig. 13(b)) geometries are illustrated. For all the results explained ahead it was assumed that $\nu = 0.31$ and $L = 10000$ units where L is the edge length of the cube or the encompassing cube

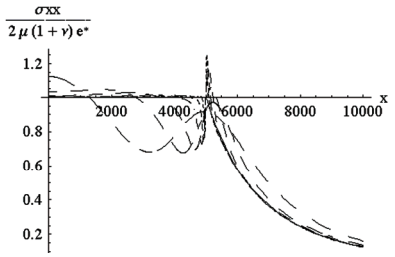


Fig. 11 Normalized σ_{xx} plotted along *x*-direction for loop densities varying from $2 \times 2 \times 2$ to $80 \times 80 \times 80$.

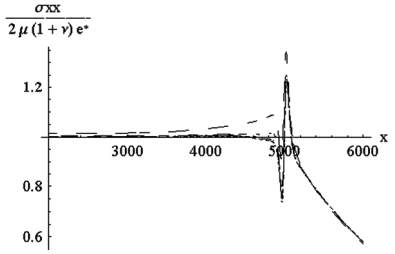


Fig. 12 Comparison of normalized σ_{xx} plotted along *x*-direction for varying number of segments per loop. Loop density for each curve is $80 \times 80 \times 80$.

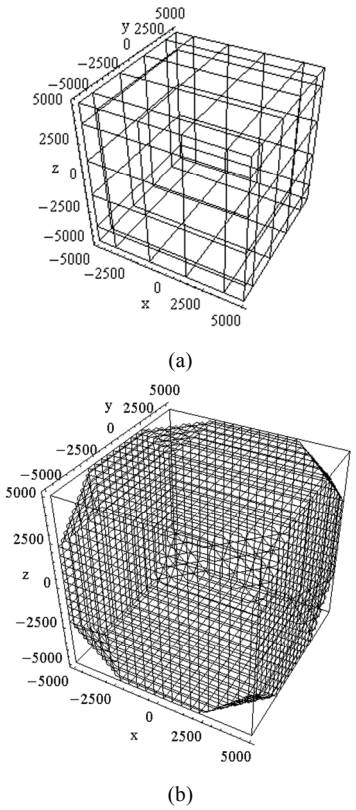


Fig. 13 (a) A mesh of square loops is generated along all the three axes using the software Mathematica ($4 \times 4 \times 4$ loop mesh). (b) A cuboidal precipitate ($20 \times 20 \times 20$ loop mesh) with uniform chamfer at the corners. The chamfer cut length is uniform and is 25% of the total face to face distance (*i.e.* edge length of an enclosing cube). These cuboidal shapes are emulated at the corners using octagonal loops. The square loops are used in between corners as in the case of perfect cube.

https://doi.org/10.1017/jmech.2014.85 Published online by Cambridge University Press

(in case of cuboidal geometry). The obtained results were normalized because the available analytical solutions were also in normalized form, where the same normalization factor from the sphere results was utilized here.

Results were first compared with available analytical results for the perfect cube (Mura, [34]). For verification of the numerical results with available analytical solutions, the square dislocation loops were first distributed along the x-direction only, *i.e.* the eigenstrain present was ε^*_{xx}. The eigenstrain considered was ε^*_{xx} because the analytical results were available for this eigenstrain. Results were obtained for different loop densities *i.e.* 2 × 2 × 2, 4 × 4 × 4, 8 × 8 × 8, 20 × 20 × 20, 40 × 40 × 40 and 80 × 80 × 80 loops. In the plots it was clear that the numerical solution converged towards the analytical solution with increasing loop densities. All the plots demonstrating this are omitted here for brevity. Now being assured of the validity of the distributed dislocation method, the numerical approach is extended to calculate results for a volume misfit (*i.e.* uniform eigenstrains are simulated using distributed dislocation loops along all the three coordinate axes, $\varepsilon^*_{xx} = \varepsilon^*_{yy} = \varepsilon^*_{zz} = \varepsilon^*$).

Figure 14 shows the plot for normalized σ_{yz} for perfect cube and chamfered corners cuboidal geometry (both at the highest loop discretization). The stress magnitude is clearly different for the two cases throughout the plot range along the x-direction. The difference becomes more significant in Figs. 15 and 16 as the chamfered corner is approached at 2500 units. Similarly, the plot for normalized σ_{xz} show the effect of chamfered geometry on the magnitude, although in this case, the magnitude difference is not as distinguishable as it was for σ_{xy} and σ_{yz} (Plots not shown). Hence, from our results so far, we can say that the effect of chamfered cuboidal geometries is not quite significant unless we are in close proximity to the chamfered corners.

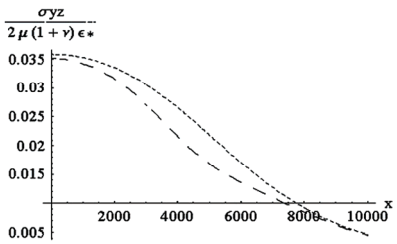


Fig. 14 Normalized σ_{yz} plotted along the x-direction for perfect cube and cuboidal shape with 25% chamfer. (y = 2500 units, z = 1000 units).

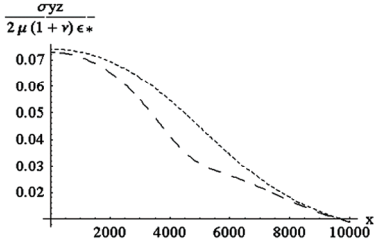


Fig. 15 Normalized σ_{yz} plotted along the x-direction for perfect cube and cuboidal shapes with 25% chamfer. (y = 2500 units, z = 2000 units).

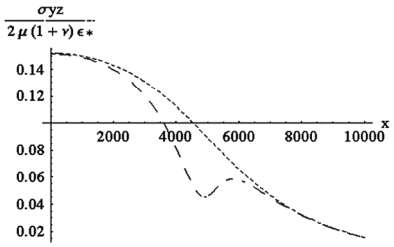


Fig. 16 Normalized σ_{yz} plotted along the x-direction for perfect cube and cuboidal shape with 25% chamfer. (y = 2500 units, z = 4000 units).

3.3 Two-Dimensional Particle in Half Space: Cylindrical and Elliptical Inclusions

3.3.1 Cylindrical Inclusion

The distributed dislocation method is now used to solve the cylindrical inclusion problem depicted in Fig. 6. An initial test was performed with the objective of analyzing the effect of variations of the mesh (discretization) size. Results were computed for an arbitrarily selected cylindrical inclusion of radius $r_0 = 100b$ ($b = 1$), $\nu = 0.3$, radial misfit $\delta = b$, and at a distance $d = 2r_0$ below the surface. The various mesh sizes used were 2 × 2, 8 × 8, 16 × 16, 30 × 30, 50 × 50, 100 × 100, and 200 × 200. The displacement along the y direction, u_y, was calculated on the surface along (x, 0), where $x \to (-400, +400)$, for the said particle discretizations and the results are shown in Fig. 17(a). Here the number of dashes increases, and their size decreases, as the mesh is refined. From the figure it is observed that convergence to a particular curve is occurring as the mesh size increases. From this specific test it was also ascertained that no appreciable improvement (less than 1%) in the results is acquired when discretizing into meshes greater than 30 × 30. Figure 17(b) shows a contour plot of the free surface using the same parameters as before and a 50 × 50 mesh.

Having established what mesh sizes yield the optimum results, it was then decided to investigate the effect the particle location would induce on the results, thus plots of the displacement u_y at the surface were obtained for increasing particle depths. For this test the cylindrical particle was again discretized into a 50 × 50 mesh and the depths used ranged from $d = r_0$ to $d = 100000r_0$. The results are shown on Fig. 18(a). Similar to the previous plots, here the number of dashes increases, and their size decreases, as d increases. As expected, the displacement at all points along the surface approach zero as the particle is placed further away from it (*i.e.*, $u_y \to 0$ as $d \to \infty$). This is due to saint Venant's principle, which basically states that the effect of the forces, due to the particle in this case, become insignificant at sufficiently large distances away from it. When the particle is at a distance $d = r_0$ underneath the free surface, the displacement u_y on the surface reaches a maximum of approximately 2. This was also expected

https://doi.org/10.1017/jmech.2014.85 Published online by Cambridge University Press

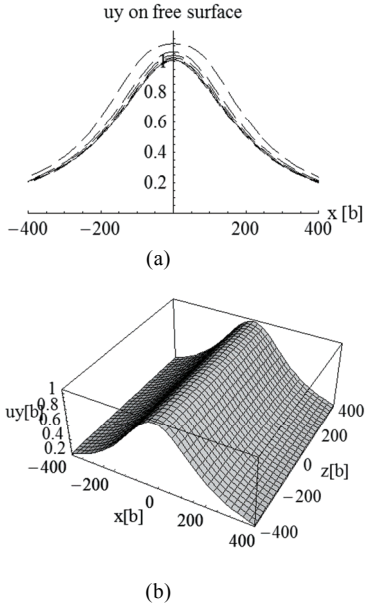


Fig. 17 (a) Displacement at free surface generated by a cylindrical inclusion of $r_0 = 100b$ at a depth $d = 2r_0$ for various discretizations. (b) Free surface contour caused by said cylindrical inclusion discretized into a 50 × 50 mesh.

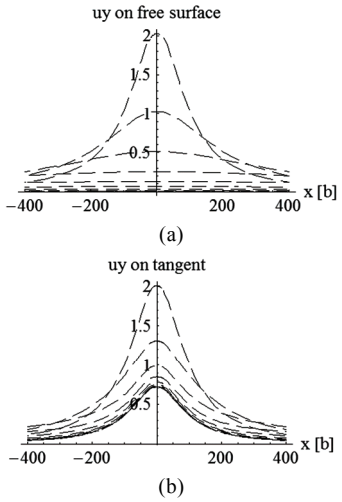


Fig. 18 (a) Displacement u_y at the free surface as d increases. (b) u_y along representative internal tangent for increasing values of d. Refer to Fig. 6(a) for internal tangent. Results generated by a cylindrical inclusion discretized into a 50 × 50 mesh.

since there is a continuous radial misfit of 1 around the particle and there is no material above the particle to restrict the displacement. Plots were also obtained along an internal line tangent to the particle, and parallel to the free surface, as d was increased. The dashed line in Fig. 6(a) represents one said plotting range. Analytical results along one such line for a particle in an infinite matrix were also obtained for comparison. As $d \rightarrow \infty$ it was anticipated that u_y would converge to the analytical solution of the particle in the infinite space, and indeed this is what the numerical results, shown in Fig. 18(b), demonstrate.

Because in the current numerical method the particles of interest are simulated with sets of orthogonal dislocation loops, it was decided to investigate if the misfit, and thus the total displacement, was uniform and in the radial direction all around the particle for the case of the cylindrical inclusion located far away from the free surface. Because of the particle symmetry, the total displacement was only computed along an arbitrarily selected portion of the particle boundary, *i.e.* (R, θ), where $R = r_0 = 100b$ and $\theta = (0, \pi/2)$. The results are shown in Fig. 19(a), in which $x = R^*\text{Cos}(\theta)$. From this figure it is evident that the total displacement is indeed constant all around the particle at any given constant distance R away from its center. As for the direction of such displacement, the angle of the displacement direction was plotted and compared with the particle boundary normal angle along the previously described boundary region. Such angles are relative to the x-axis. The resulting plots are shown in Fig. 19(b), where it is noticed that the curves for the displacement angle (dashed) and the particle boundary normal angle (solid) overlap. This is crucial evidence showing that the displacement is in the radial direction as expected. As trivial as the plots in Fig. 19 may seem, they aid in proving that the numerical method presented here can accurately simulate two dimensional volume misfit problems.

Furthermore, for the numerical results to be valid satisfaction of the equilibrium equations has to occur. Figure 20 demonstrates satisfaction of one equilibrium equation over $x \rightarrow (-200, 200)$ and $y \rightarrow (0, -400)$. Again, the cylindrical particle used in these calculations was discretized into a 50 × 50 mesh, and $d = 2r_0$. Plots of the traction on the surface were also obtained, and as required, the condition of zero traction on the surface was satisfied.

3.3.2 Elliptical Inclusion

Results were also computed and plotted for the case of an elliptical inclusion. Here, the dimensions of the particle were arbitrarily selected to be: $a_1 = 200b$ (half-major-axis) and $a_2 = 100b$ (half-minor-axis), as shown in Fig. 21. This particle was discretized with a total of 60 loops along the x axis and 30 loops along the y axis, *i.e.* a 60 × 30 mesh, also shown in Fig. 21.

In this particular case the true volume misfit problem, where the particle and the void possess identical geometries but are slightly different in size, dictates that the misfit around the particle boundary is not uniform. This means that if δy is arbitrarily chosen to be 1.5 then δx must be equal to 3 because of the chosen elliptical particle dimensions, *i.e.* the 2:1 aspect ratio of the major and minor axes. Such values for the total directional misfits were chosen for the calculations that following. Figures 22(a) and 22(b) show the displacement u_y along the free surface and along an internal tangent to the particle (see Fig. 6(a)), respectively, as d gradually increased. In Fig. 22(a) it is again evident that as d increases, u_y on the free surface approaches zero as anticipated.

https://doi.org/10.1017/jmech.2014.85 Published online by Cambridge University Press

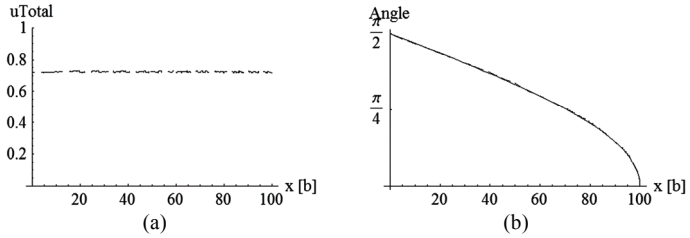


Fig. 19 (a) Total displacement magnitude at cylindrical particle boundary. (b) Angle of particle boundary normal (solid line) and angle of total displacement (dashed line) at cylindrical particle boundary.

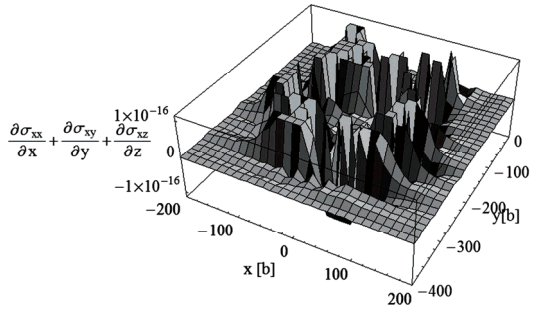


Fig. 20 This figure shows satisfaction of one of the equilibrium equations.

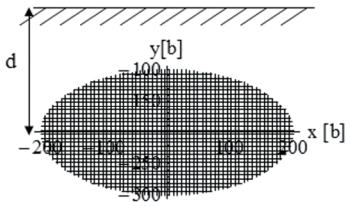


Fig. 21 Elliptical particle at a distance d underneath a free surface. The particle has been discretized into a 60 × 30 mesh.

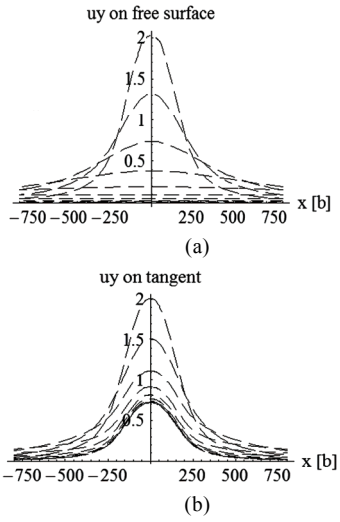


Fig. 22 (a) Displacement u_y at free surface as d increases. (b) u_y along tangent to particle for increasing value of d. Refer to Fig. 6(a) for representation of tangent. Results generated by an elliptical inclusion discretized into a 60 × 30 mesh.

The total displacement along a representative portion of the elliptical particle boundary was plotted next and the results are shown in Fig. 23(a). In the figure it can be seen that the total displacement magnitude is constant. Only when we plotted the angle of the total displacement and the angle of the boundary normal was it evident that at any specific point, except at the extremes, the angle of the displacement was lower than the angle of the normal. This is observed in Fig. 23(b), where the solid line represents the boundary normal angle. These findings suggest that the displacement is more pronounced toward the direction where the total linear misfit is greater, which in this case is in the x-direction. Plots demonstrating satisfaction of the equilibrium equations and plots demonstrating zero traction on the free surface were also obtained but are not presented here for brevity.

Results from a cylindrical inclusion were also analyzed against those from an elliptical one in order to compare the variation in the free surface displacement due to the two inclusion configurations. As previously, both inclusions were located at a distance $d = 100b$ beneath the free surface, the radius of the cylindrical inclusion was $r_0 = 100b$, the dimensions of the elliptical inclusion were $a_1 = 200b$ and $a_2 = 100b$, and their discretizations were 50 × 50 and 60 × 30, respectively. The resulting y displacement plots at the free surface are depicted in Fig. 24, where the solid line represents the elliptical inclusion and the dashed line represents the cylindrical one. As expected, the curve for the elliptical inclusion is wider than that of the cylindrical one due to its broader shape.

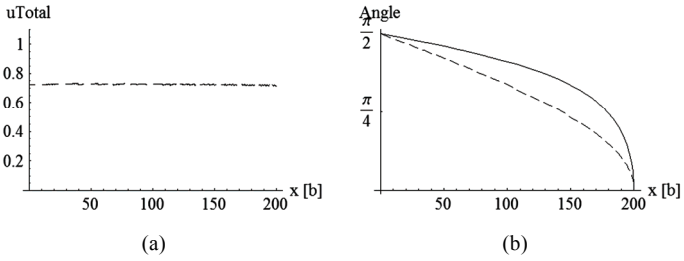


Fig. 23 (a) Total displacement at section of particle boundary, (b) Angle of particle boundary normal (solid line) and angle of displacement (dashed line) at elliptical particle boundary.

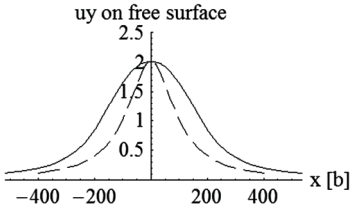


Fig. 24 Comparison of y displacement at free surface due to elliptical inclusion (solid line) and cylindrical inclusion (dashed line) at a distance $d = 100b$ beneath the free surface.

https://doi.org/10.1017/jmech.2014.85 Published online by Cambridge University Press

4. CONCLUSIONS

In this document, we have introduced an innovative numerical method by which to obtain the elastic fields generated by two and three dimensional volume misfit inclusions in an infinite space and two dimensional inclusions in a half-space. The method consists of discretizing the inclusion into perpendicular planes of atoms via dislocation lines. As shown here, solutions obtained with this method seems to agree superbly with existing analytical solutions of simple particles. This method may be extended in order to have the capability of solving for three dimensional inclusions in half-space. Also, because the method is dislocation-based, it could readily be incorporated into existing dislocation dynamics codes for more advanced studies.

ACKNOWLEDGEMENTS

The authors would like to thank Pei Jing whose work helped with this manuscript.

FINANCIAL SUPPORT

The authors acknowledge the DOE Lawrence Livermore National Laboratory (LLNL) and the DOD AFOSR as partial financial supporters for this work.

REFERENCES

1. Teodosiu, C., *Elastic Models of Crystal Defects*, Springer-Verlag, Berlin, Germany (1982).
2. Bert, N. A., Kolesnikova, A. L., Romanov, A. E. and Chaldyshev, V. V., "Elastic Behavior of a Spherical Inclusion with a Given Uniaxial Dilatation," *Physics of the Solid State*, **44**, pp. 2139–2148 (2002).
3. Eshelby, J. D., "The Determination of the Elastic Field of an Ellipsoidal Inclusion, and Related Problems," *Proceedings of the Royal Society of London Series A*, **221**, pp. 376–396 (1957).
4. Eshelby, J. D., "Elastic Field Outside an Ellipsoidal Inclusion," *Proceedings of the Royal Society of London Series A*, **252**, pp. 561–569 (1959).
5. Pearson, G. S. and Faux, D. A., "Analytical Solution for Strain in Pyramidal Quantum Dots," *Journal of Applied Physics*, **88**, pp. 730–736 (2000).
6. Andreev, A. D., Downes, J. R., Faux, D. A. and O'Reilly, E. P., "Strain Distribution in Quantum Dots of Arbitrary Shape," *Journal of Applied Physics*, **86**, pp. 297–305 (1999).
7. Sheinerman, A. G. and Ovid'ko, I. A., "Elastic Fields of Inclusions in Nanocomposite Solids," *Reviews on Advanced Materials Science*, **9**, pp. 17–33 (2005).
8. Melan, E., "Der Spannungszustand Der Durch Eine Einzelkraft Im Innern Beanspruchten Halbscheibe," *Journal of Applied Mathematics and Mechanics*, **12**, pp. 343–346 (1932).
9. Mindlin, R. D., "Force at a Point in the Interior of a Semi-Infinite Solid," *Journal of Applied Physics*, **7**, pp. 195–202 (1936).
10. Mindlin, R. D. and Cheng, D. H., "Nuclei of Strain in the Semi-Infinite Solid," *Journal of Applied Physics*, **21**, pp. 926–930 (1950a).
11. Mindlin, R. D. and Cheng, D. H., "Thermoelastic Stress in the Semi-Infinite Solid," *Journal of Applied Physics*, **21**, pp. 931–933 (1950b).
12. Aderogba, K., "On Eigenstress in a Semi-Infinite Solid," *Mathematical Proceedings of the Cambridge Philosophical Society*, **80**, pp. 555–562 (1976).
13. Chiu, Y. P., "On the Stress Field and Surface Deformation in a Half Space with a Cuboidal Zone in Which Initial Strains Are Uniform," *Journal of Applied Mechanics*, **45**, pp. 302–306 (1978).
14. Hu, S. M., "Stress from a Parallelepipedic Thermal Inclusion in a Semispace," *Journal of Applied Physics*, **66**, pp. 2741–2743 (1989).
15. Seo, K. and Mura, T., "The Elastic Field in a Half Space Due to Ellipsoidal Inclusions with Uniform Dilatational Eigenstrains," *Journal of Applied Mechanics*, **46**, pp. 568–572 (1979).
16. Masmura, R. A. and Chou, Y. T., "Antiplane Eigenstrain Problem of an Elliptic Inclusion in an Anisotropic Half Space," *Journal of Applied Mechanics*, **49**, pp. 52–54 (1982).
17. Hasegawa, H., Lee, V. G. and Mura, T., "Hollow Circular Cylindrical Inclusion at the Surface of a Half-Space," *Journal of Applied Mechanics*, **60**, pp. 33–40 (1993).
18. Wu, L. Z. and Du, S. Y., "The Elastic Field in a Half-Space with a Circular Cylindrical Inclusion," *Journal of Applied Mechanics*, **63**, pp. 925–932 (1996).
19. Ru, C. Q., "Analytic Solution for Eshelby's Problem of an Inclusion of Arbitrary Shape in a Plane or Halp-Plane," *Journal of Applied Mechanics*, **66**, pp. 315–322 (1999).
20. Glas, F., "Coherent Stress Relaxation in a Half Space: Modulated Layers, Inclusions, Steps, and a General Solution," *Journal of Applied Physics*, **70**, pp. 3556–3571 (1991).
21. Glas, F., "Elastic Relaxation of Truncated Pyramidal Quantum Dots and Quantum Wires in a Half Space: An Analytical Calculation," *Journal of Applied Physics*, **90**, pp. 3232–3241 (2001).
22. Glas, F., "Analytical Calculation of the Strain Field of Single and Periodic Misfitting Polygonal Wires in a Half-Space," *Philosophical Magazine A*, **82**, pp. 2591–2608 (2002).
23. Glas, F., "Elastic Relaxation of Isolated and Interacting Truncated Pyramidal Quantum Dots and Quantum Wires in a Half Space," *Applied Surface Science*, **188**, pp. 9–18 (2002b).
24. Glas, F., "Elastic Relaxation of a Truncated Circular Cylinder with Uniform Dilatational Eigenstrain in a Half Space," *Physical Status Solidi*, **237**, pp. 599–610 (2003).

https://doi.org/10.1017/jmech.2014.85 Published online by Cambridge University Press

25. Romanov, A. E., Beltz, G. E., Fischer, W. T., Petroff, P. M. and Speck, J. S., "Elastic Fields of Quantum Dots in Subsurface Layers," *Journal of Applied Physics*, **89**, pp. 4523–4531 (2001).
26. Pan, E. and Yang, B., "Elastostatic Fields in an Anisotropic Substrate Due to a Buried Quantum Dot," *Journal of Applied Physics*, **90**, pp. 6190–6196 (2001).
27. Hirth, J. P. and Lothe, J., *Theory of Dislocations,* Krieger Publishing Company, Florida, U.S., pp. 86–88 (1982).
28. Hull, D. and Bacon, D. J., *Introduction to Dislocations*, Butterworth-Heinemann, Oxford, U.K., pp. 77–78 (1984).
29. Lerma, J., Khraishi, T., Shen, Y. L. and Wirth, B. D., "The Elastic Fields of Misfit Cylindrical Particles: A Dislocation-Based Numerical Approach," *Mechanics Research Communications*, **30**, pp. 325–334 (2003).
30. Devincre, B., "Three-Dimensional Stress-Field Expressions for Straight Dislocation Segments," *Solid State Communications*, **93**, pp. 875–878 (1995).
31. Bacon, D. and Groves, P. T., "The Dislocation in a Semi-Infinite Isotropic Medium," *Fundamental Aspects of Dislocation Theory*, **1**, pp. 35–45 (1970).
32. Jing, P., "Modeling Irradiation Damage in Crystalline Solids," M.S. Thesis, University of New Mexico, New Mexico, U.S. (2003).
33. Weertman, J., *Dislocation Based Fracture Mechanics*, World Scientific, Singapore (1996).
34. Mura, T., *Micromechanics of Defects in Solids*, the Hague, Martinus Nijhoff Pub., the Netherlands (1982).

(Manuscript received April 23, 2014,
accepted for publication July 17, 2014.)

https://doi.org/10.1017/jmech.2014.85 Published online by Cambridge University Press